# Understanding the effect of turbulent structures on three-dimensional sphere motions in boundary layers

Yi Hui Tee[1,2,*], Ellen K. Longmire[1]

1: Dept. of Aerospace Engineering and Mechanics, University of Minnesota, U.S.A.
2: Dept. of Energy and Process Engineering, Norwegian University of Science and Technology, Norway
*Corresponding author: teexx010@umn.edu

**Keywords: Particle-laden flow, Particle tracking, Large-scale coherent structures, Lift force**

## ABSTRACT

This paper extends the research by Tee et al. (2020) and Tee & Longmire (2021) to investigate the effect of turbulent activity on the wall-normal motion of spheres with specific gravities of 1.006 (P1) and 1.152 (P3) at $Re_\tau = 670$ and 1300. These spheres extend into the logarithmic region with $d^+ = 56$ and 116. Both sphere and fluid motions were tracked simultaneously using separate techniques; 3D particle tracking was used to track the individual spheres over a streamwise distance of 5 boundary layer thicknesses while stereoscopic particle image velocimetry was implemented to track the fluid motion surrounding the spheres over streamwise-spanwise planes at multiple streamwise and wall-normal locations. Upon release, sphere P1 accelerated strongly and lifted off of the wall due to strong mean shear before descending back towards the wall at both $Re_\tau$. Then, the sphere either ascended again without returning to the wall or else contacted the wall and slid before lifting off again. This sphere did not develop any significant rotations throughout its trajectory. The subsequent lift-offs observed, which were of similar or larger magnitude to the initial lift-offs, were prompted by fluid upwash and/or temporary increases in shear lift due to passing high momentum zones. While ejection events were found to be important to sphere lift-offs, we did not observe any distinct fluid structures or sweep motions associated with sphere descents. These descents were likely dominated by gravity after the positive lift on the sphere decreased following its detachment from the wall. The upward impulse from Q2 type events was limited, and once the sphere moved away from the wall, the upward shearing lift was insufficient to keep the sphere suspended. The denser sphere P3, by contrast, did not lift off upon release and initially slid along the wall while lagging the fluid significantly. After it had propagated approximately $1.5\delta$ downstream, it began rolling forward (while slipping) and accelerated again. The forward rotation induced sufficient Magnus lift to generate small lift-off events of magnitude $\leq 0.2d$ repeating at relatively high frequency independent of the larger turbulence structures around the sphere.

## 1. Introduction

Particle-laden turbulent flows are commonly seen in various applications ranging from aerospace and industry to the environment. These particles might be ice or dust in the air, or alternatively

sediment, plankton, or pollutants in the ocean where the flows are turbulent in nature. They can either slide or roll along the bounding surface and lift-off from or collide with the wall due to their complicated interactions with coherent structures in the boundary layer and wall friction. Particle-turbulence and particle-wall interactions can have significant impacts on the suspension, deposition and transport of these particles, but currently, the understanding of these effects is limited.

Research investigating particle-laden flow is challenging due to the complexity in modeling or re-constructing both fluid and particle motions across a wide range of length scales (Brandt & Coletti, 2021). In many earlier numerical simulations, particles were modeled as point-masses with no vol-ume and thus no rotation to simplify the problem (Soldati & Marchioli, 2009). However, a study by Costa et al. (2020) comparing the results between interface-resolved and one-way-coupled point-particle direct numerical simulations (DNS) demonstrated distinctive differences in particle be-havior near the wall due to the absence of any shear-induced lift force in the point-particle model. Without the supplement of experimental data in understanding the particle motion, it is challeng-ing to model these motions accurately.

In the context of experimental studies, early work examining particle wall-normal motion in tur-bulent open-channel flows included imaging experiments from Sutherland (1967), Francis (1973), and Sumer & Oğuz (1978), to name a few. Later, van Hout (2013), Ahmadi et al. (2019), and Baker & Coletti (2021), among others, incorporated direct visualization techniques to measure particle and fluid velocities. These studies concluded that particle resuspension events are strongly influ-enced by the near-wall turbulence activities, namely the ejection events. However, these previous studies have been limited to investigation of the translation of small inertial particles without con-sideration of particle rotation.

For a fixed particle near the wall, Zeng et al.'s (2008) DNS results demonstrated that the mean lift forces on spheres with diameters $1.78 \leq d^+/2 \leq 12.47$ centered at a wall-normal location $y^+ = 17.31$ from the wall at friction Reynolds number, $Re_\tau = 178.12$ were negative in all cases. From here onward, the superscript + denotes quantities normalized by the friction velocity ($u_\tau$) and the kine-matic viscosity ($\nu$). Tomographic particle image velocimetry (PIV) performed by van Hout et al. (2018) at $Re_\tau = 352$ downstream of a tethered sphere with $d^+/2 = 25$ centered at $y^+ = 43$ above the wall also reported a similar observation due to the sphere wake tilting away from the wall. By contrast, Hall (1988), who measured the mean lift force acting on a stationary particle attached to the wall in a turbulent boundary layer using a force transducer, reported a positive lift contri-bution. The experimental data showed that for $3.6 < d^+ < 140$ and particle Reynolds number, $6.5 < Re_p < 1250$, the normalized mean lift forces were strongly positive and could be approx-imated by $F_L^+ = (20.90 \pm 1.57)(d^+/2)^{2.31 \pm 0.02}$. These results imply that the net wall-normal force including lift related to the mean shear can vary significantly with the sphere position relative to the wall. For a larger particle whose diameter extends into the logarithmic layer, instantaneous lift forces associated with large-scale coherent structures such as alternating high and low momentum regions (Ganapathisubramani et al., 2003; Tan & Longmire, 2017) may play important roles due to

significant variations in the local streamwise velocity gradient.

As mentioned above, rotation-induced Magnus lift on particles remains relatively unstudied mainly due to the added challenges in reconstructing or modeling particle rotation. Current experimental methods for reconstructing sphere orientation include printing specific patterns over the sphere surface (Zimmermann et al., 2011; Mathai et al., 2016) and embedding visible tracers into the interior of transparent spheres (Bellani et al., 2012; Klein et al., 2013). The former method compares the unique pattern captured by high-speed cameras with synthetic projections to extract the absolute sphere orientation; the latter method resolves tracer velocities within the solid body to obtain the rotation rate. Barros et al. (2018) extended Klein et al.'s (2013) methodology to include opaque spheres. Small dots were marked all over the solid surface, and two cameras were employed to reconstruct the 3D rotation rate using Kabsch's (1976) algorithm.

In this paper, we extend Tee et al.'s (2020) study on three-dimensional sphere motions in turbulent boundary layers by conducting simultaneous stereoscopic particle image velocimetry and three-dimensional sphere tracking experiments to investigate the instantaneous fluid motion surrounding a moving sphere. Barros et al.'s (2018) methodology is adapted to the requirements of the current experimental setup to obtain both the translation and rotation of a sphere. Multiple sphere densities and flow conditions are considered. The results are analyzed to investigate the coupling between the spheres and the surrounding fluid motion and to understand the dynamics of sphere lift-offs and descents.

## 2. Methodology

The experiments were performed in a recirculating water channel with a turbulent boundary layer developing along the bottom wall. The channel test section, which is constructed of glass, is 8 m long and 1.12 m wide. Hereafter, $x$, $y$ and $z$ define the streamwise, wall-normal and spanwise directions. We consider two friction Reynolds numbers, $Re_\tau$=670 and 1300 with boundary layer thicknesses, $\delta$=76 and 71 mm and respectively. The corresponding free-stream velocities ($U_\infty$) were 0.205 and 0.464 m s$^{-1}$, The water depths were maintained at 0.396 m and 0.392 m respectively. The mean flow statistics of the unperturbed turbulent boundary layers were determined from planar PIV measurements in streamwise wall-normal planes (see Tee, 2021).

Individual magnetic wax spheres with diameter, $d$ = 6.35 mm and specific gravities of 1.006 (P1) and 1.152 (P3) were released from rest on a smooth wall. These spheres were made in-house from a mixture of wax and iron oxide using molds. A given sphere was positioned initially at a location 4.2 m downstream of the trip wire and $4\delta$ away from the nearest sidewall. This location will be considered as the origin in $x$ and $z$, with the bottom wall as $y$ = 0. For each run, the sphere was held at rest by a magnet flush with the outer channel wall. By deactivating the solenoid, the magnet moved away from the wall, and the sphere was released to propagate with the incoming flow. A screen was located at the end of the test section to capture the sphere and prevent it from recirculating around the channel.

*(a)*

*(b)*
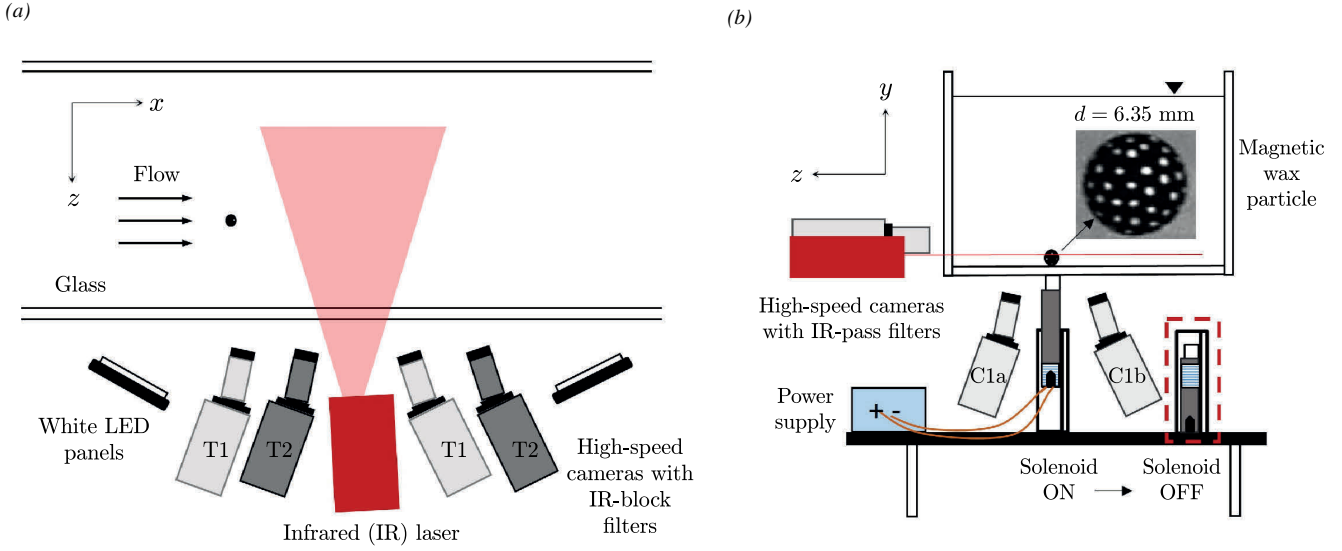


**Figure 1.** Schematic of experimental setup. *(a)* Top view: two pairs of high-speed cameras (T1 and T2) with infrared-block filters, aligned in stereoscopic configurations for capturing the trajectory and rotation of a marked sphere over a long field of view. *(b)* Cross-section view: one pair of stereoscopic high-speed cameras (C1a and C1b) with infrared-pass filters, positioned under channel to capture fluid motion in the streamwise-spanwise plane illuminated by the infrared laser. The sphere was held in place by a magnet attached to a solenoid. Inset: example of sphere captured in gray-scale with diameter spanning $\sim 43$ pxs or 6.35 mm.

The sphere diameters were significantly larger than the Kolmogorov length scale, with $d^+$ of 56 and 116 respectively. The initial particle Reynolds numbers, $Re_p = U_{rel}d/\nu$ at both mean flow conditions were 730 and 1730 respectively, where $U_{rel}$ defines the relative velocity between sphere and mean fluid at the initial sphere center location and $\nu$ is the kinematic viscosity of water at 20°C. Meanwhile, the particle Stokes numbers ($St^+$, $St_\delta$) expressed as the ratio of particle response time, $\tau_p = (\rho_f + 2\rho_p)d^2/36\nu\rho_f$ (Crowe, 2005) to the characteristic flow time scale based on viscous time scale ($\nu/u_\tau^2$) and largest time scale ($\delta/U_\infty$), range from 262 to 1230 and 9.1 to 23.5, respectively. Details of the experimental parameters are summarized in Table 1.

To track the sphere translation and rotation, the methodology and reconstruction method proposed

**Table 1.** Summary of experimental parameters. $|V_s|$ represents sphere settling velocity magnitude in quiescent flow; $\overline{F_L}^* = (\overline{F_L} - F_b)/F_b$ where $\overline{F_L}$ and $F_b$ denote the mean wall-normal fluid-induced force based on Hall's (1988) expression and the net buoyancy force, respectively.

| $Re_\tau$ | Initial $Re_p$ | $d^+$ | Sphere | $\rho_p/\rho_f$ | $|V_s|/U_\infty$ | $St^+$ | $St_\delta$ | Initial $\overline{F_L}^*$ |
|---|---|---|---|---|---|---|---|---|
| 670 | 730 | 56 | P1 | 1.006 | 0.083 | 262 | 9.10 | $11 \pm 2$ |
| | | | P3 | 1.152 | 0.78 | 287 | 9.98 | $-0.77 \pm 0.04$ |
| 1300 | 1730 | 116 | P1 | 1.006 | 0.037 | 1120 | 21.4 | $61 \pm 10$ |
| | | | P3 | 1.152 | 0.34 | 1230 | 23.5 | $0.24 \pm 0.2$ |

by Barros et al. (2018) was employed. Small dots were painted all over the sphere surface using a white oil-based pen. The spheres were tracked in a three-dimensional space using two pairs of stereoscopic high-speed cameras (Phantom v210 from Vision Research Inc.) over a streamwise distance of approximately $5\delta$ (see Figure 1*a*). White LED panels were used to illuminate the domain. Before computing the particle translation and rotation, the gray-scale images were pre-processed with a Matlab circular Hough Transform routine to isolate the sphere from the background. The extracted sphere images were then imported to Davis 10.1 and further processed with 3 x 3 Gaussian smoothing and sharpening routines to increase the dot contrasts. Subsequently, pixel intensity values that were less than the white dots were set to 0 to isolate the dots from the sphere image. After performing a volumetric calibration, a 3D-PTV routine was implemented to reconstruct the dot coordinates from both camera pairs. As only two cameras were used in each 3D-PTV reconstruction, the data sets consisted of the 3D coordinates of true and ghost markers and their corresponding 3D velocity vectors. Hence, knowing that the true markers were limited in depth over the sphere radius in the spanwise direction and should lie on the sphere surface, the filtering methodology proposed by Barros et al. (2018) was employed to remove the ghost tracks. Once the true markers were identified, the sphere centroid was determined by applying the equation of a sphere to obtain the sphere translation. Then, a rotation matrix that best aligned the markers of consecutive images was obtained to reconstruct the sphere angular velocity and orientation.

To track the fluid motion, stereoscopic particle image velocimetry (SPIV) experiments were conducted using two Miro 110 high-speed cameras (Vision Research Inc.) positioned under the channel (see Figure 1*b*). The flow was seeded with 13-micron silver-coated hollow glass beads. An Oxford Firefly 300W infrared laser (wavelength: 808 nm), aimed through the side wall, illuminated an $x - z$ plane in the flow field. The laser sheet thickness was 1 mm. Here, infrared-block and pass optical filters were mounted to the lenses of the tracking and PIV cameras, respectively. All six cameras were triggered simultaneously at the same frequency to capture both sphere and fluid motions. To cover different fluid regions surrounding the spheres throughout their trajectories, the SPIV experiments were repeated at two streamwise and wall-normal locations corresponding with $y/d = 0.7$ ($y^+ = 40$ and 80) and $y/d = 1.4$ ($y^+ = 80$ and 160) as summarized in Table 2. Stereoscopic self-calibration was carried out on top of the classic calibration at each location using 200 image pairs from the unperturbed flow fields. At each laser sheet position, for each case considered, up to $J = 10$ sphere trajectories and fluid flow fields were captured using the same sphere.

Prior to processing the SPIV images in Davis 10.1, the sphere, which appeared as a very bright spot, was removed using Matlab. Then, the spatial auto-mask function in Davis 10.1 was implemented to mask out regions without tracer particles such as the sphere location and its shadow. Sliding sum-of-correlation with a filter length of 2 images, and an overlap of 50% over initial interrogation window sizes of 64 by 64 pixels followed by three passes of 32 by 32 pixels was then employed to obtain the three-component velocity vectors (see Sciacchitano et al., 2012). The spatial resolutions of the computed SPIV velocity vectors (based on the final interrogation window of 32 pxs) were 24 and 50 viscous units at $Re_\tau$ of 670 and 1300, equivalent to 2.73 mm. A detailed explanation on the experimental setup can be found in Tee (2021).

**Table 2.** Summary of SPIV measurements.

| Position | $x$ | $y$ | $z$ | $\overline{U_o(y_{spiv})}$ [m s$^{-1}$] | |
|---|---|---|---|---|---|
| | | | | $Re_\tau = 670$ | $Re_\tau = 1300$ |
| A | $0.3 < x/\delta < 1.7$ | $0.7d$ | $-0.45 < z/\delta < 0.45$ | 0.124 | 0.287 |
| B | $0.3 < x/\delta < 1.7$ | $1.4d$ | $-0.45 < z/\delta < 0.45$ | 0.138 | 0.306 |
| C | $1.4 < x/\delta < 2.8$ | $0.7d$ | $-0.2 < z/\delta < 0.7$ | 0.124 | 0.287 |

## 3. Results and discussion

Figures 2 and 3 show the sphere wall-normal trajectory and orientation associated with forward rotation for sphere P1 (plotted in black) and P3 (plotted in purple) at $Re_\tau = 670$ and 1300 respectively. Overall, our results show that in all four cases, the spheres exhibited similar behavior to that reported in Tee et al. (2020). Readers are encouraged to refer to Tee et al. (2020) for a more detailed analysis of the three-dimensional sphere translation and rotation not covered in this paper.

Here, sphere P1 accelerated strongly and typically lifted off of the wall upon release. Owing to the stronger resultant upward force as computed using Hall's (1988) equation and listed in Table 1, this sphere lifted off to greater heights at the higher $Re_\tau$. Thus, the initial lift-off height correlated strongly with the local mean shear. After reaching a maximum height in the logarithmic region, the sphere always descended towards the wall before ascending again. As shown in Figure 3, this sphere rotated only weakly about the spanwise axis. For reference, this sphere also did not rotate much about either of the other two axes (not shown here).

On the other hand, the denser sphere P3 did not lift off upon release. Based on Hall's (1988) estimation, this sphere did not have sufficient upward force to overcome the opposing buoyancy force and thus, translated along the wall upon release at both $Re_\tau$. Also, the results in Figure 3 suggest that the sphere initially slid forward without rolling after release. After the sphere traveled downstream a finite distance, the slopes of $\theta_z$ indicate that it began to roll forward up to a constant angular velocity. Small repeated lift-off events of $\leq 0.2d$ were also observed following the forward rotation. As reported in Tee et al. (2020), these small lift-offs were associated with Magnus lift. The Magnus lift was stronger for the lower $Re_\tau$ case because the that sphere was traveling with a higher dimensionless rotation rate, e.g. the ratio of rotation to translation was higher. The relatively small heights associated with the lift-off events result from the fact that the Magnus lift was insufficient to overcome the net downward force after the sphere moved away from the wall. Note that all sphere/wall collisions were inelastic, eliminating wall rebound as a cause of lift off.

Although the forward-rotation induced Magnus lift was important for P3, it was inconsequential for sphere P1 which rotated only weakly as plotted in Figure 3. After its initial acceleration from rest, the relative velocity between sphere P1 and the surrounding fluid decreases, and the associated mean shear lift must decrease. Hence, the subsequent lift-offs, which can lead to larger wall-

*(a)*

*(b)*
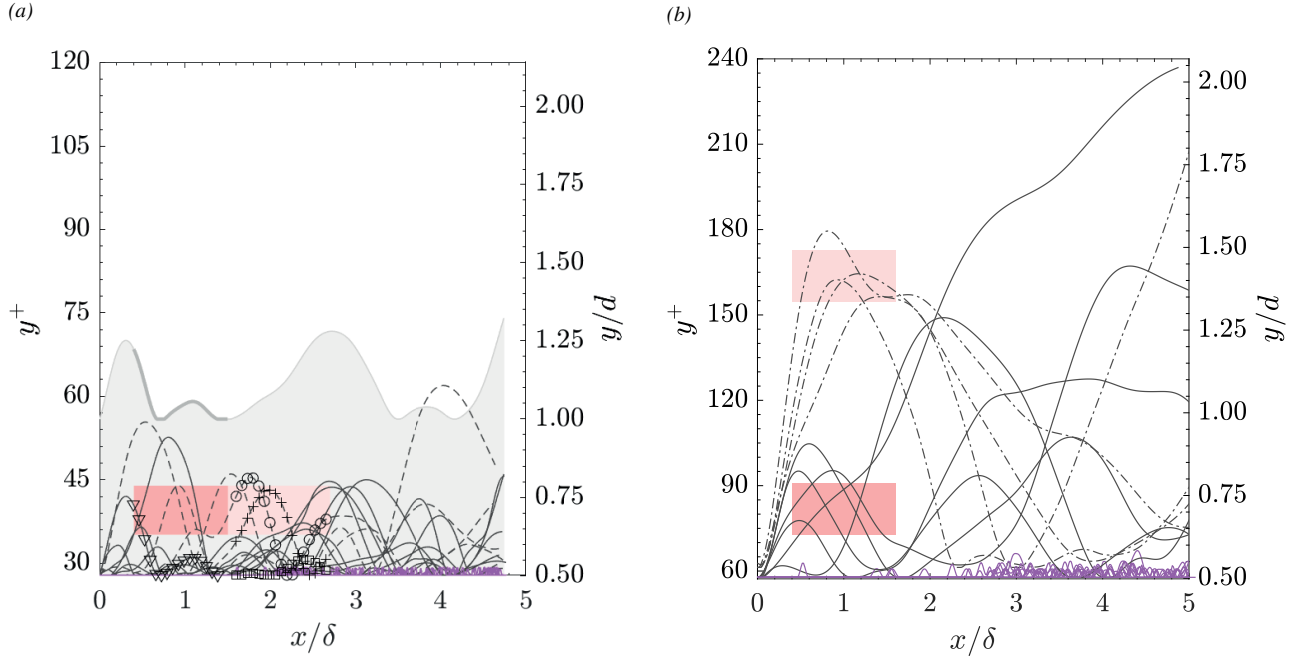
**Figure 2.** Sphere P1 (black) and P3 (purple) wall-normal trajectories plotted based on centroid location at (*a*) $Re_\tau$ = 670 and (*b*) 1300. Solid lines, dot-dashed lines, and dashed lines represent sphere trajectories corresponding with laser sheet positions A, B, and C respectively as marked by red shaded regions (see Table 2). Symbols triangle, square, circle and cross in (*a*) represent different runs depicted in Figures 4*a*, 4*b*, 6*a*, and 6*b* respectively. Here, the grey line and shaded region represent the upper half of the sphere for one sample run marked by the downward pointing triangles.

*(a)*

*(b)*
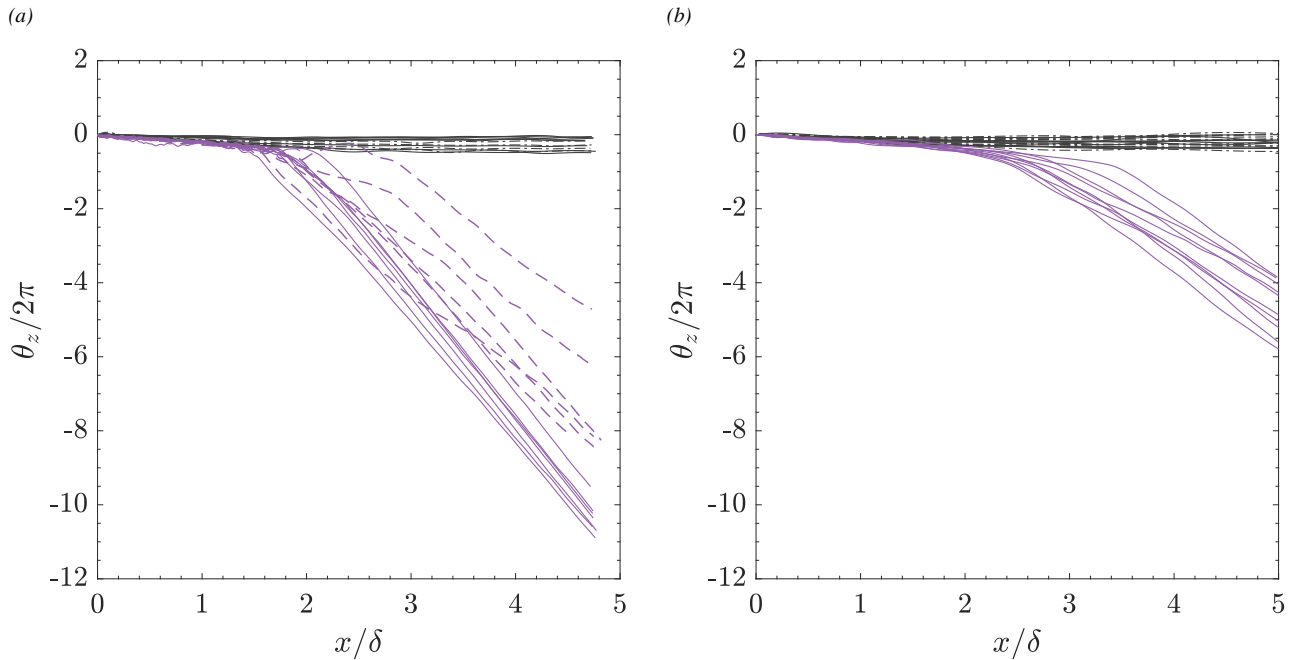
**Figure 3.** Sphere orientation about the spanwise axis at (a) $Re_\tau$ = 670 and (b) 1300. Black: sphere P1. Purple: sphere P3. Solid lines, dot-dashed lines, and dashed lines represent sphere trajectories from laser sheet positions A, B, and C respectively (see Table 2.

normal heights than the initial lift-offs (see Tee et al., 2020), must be aided by the instantaneous wall-normal force acting on the sphere due to the surrounding fluid. To understand the lift-off of a translating sphere with minimal rotation, the velocity fields surrounding the lifting sphere P1 at $Re_\tau$ = 670 are plotted in Figure 4 for two sample runs prior to lift-off. In Figure 4(a, b), the red regions represent the laser sheet location while the grey regions represent the extent of the sphere cross section based on the centroid position plotted in black. The magenta dashed lines depict the sphere streamwise position corresponding with the contour plots in Figures 4(c, e, g) and (d, f, h), which show the fluid streamwise fluctuating velocity ($u'$), wall-normal velocity ($V$), and negative Reynolds shear stress ($-u'v'$) respectively. In these contour plots, the grey regions represent the shadow under the sphere (colored in black). The signed 2D swirling strengths, plotted as black and green contours in Figures 4(c, d) to represent clockwise and counter-clockwise (positive and negative) swirls, are computed from the imaginary part of the complex eigenvalue of the local velocity-gradient tensor.

In the first example (see Figure 4a), after descending and touching the wall, the sphere first slid along the wall for a short distance of $\sim 0.1\delta$ before lifting off at $x/\delta \sim 0.7$ and then descending again. As shown in Figure 4c, prior to lifting off, the sphere is located within a hairpin packet as indicated by the long slow-moving zone colored in blue. The sphere is also surrounded by pairs of black and green swirls, indicative of hairpin legs. In Figure 4e, the sphere is surrounded by regions of upward moving fluid where $V > 0$. The corresponding $-u'v'$ plot in Figure 4g implies that the sphere is surrounded by multiple Q2 events where $u'<0$ and $v'>0$. These structures are observable across a series of frames both prior to and during the sphere lifting event. Multiple studies in the past based on streamwise-wall normal planes reported that the lift-off of a small particle from the wall is induced by an ejection event in the buffer region (e.g., van Hout, 2013; Baker & Coletti, 2021). For a sphere with larger Stokes number, our study suggests that Q2 events in the logarithm region are also important in generating the upward impulse required to lift the sphere off of the wall.

Aside from the lift force induced by the smaller scale wall-normal fluctuations, shear-induced lift associated with a local fast-moving zone is also important to the sphere lift-off events. Figure 4b shows a second example of sphere P1 at $Re_\tau$ = 670 at a location further downstream than the previous example. In this case, the sphere travels within a slow-moving zone before moving towards $-z$ and entering the neighboring fast-moving zone at $x/\delta \sim 1.9$ (see figure 4d). Although this sphere is not surrounded by Q2 events, the wall-normal fluid velocity is at least partially upward as seen in figure 4f. As this sphere propagates from the low momentum to the high momentum fluid region, the sphere Reynolds number, $Re_{(p,f)}$, estimated based on the relative streamwise velocity between the sphere and the fluid immediately upstream, increases from 170 to 240 immediately before the lift off event. In computing $Re_{(p,f)}$, the fluid velocity is averaged over the region upstream of the sphere only to avoid the velocity deficit in the wake region immediately downstream. Overall, the results for this event suggest that the sphere lifted off of the wall at $x/\delta \sim 2$ due to an increase in instantaneous shear lift prompted by the high momentum region. Thus, both streamwise and wall-normal fluid components may be important to the sphere lift off. This result also highlights
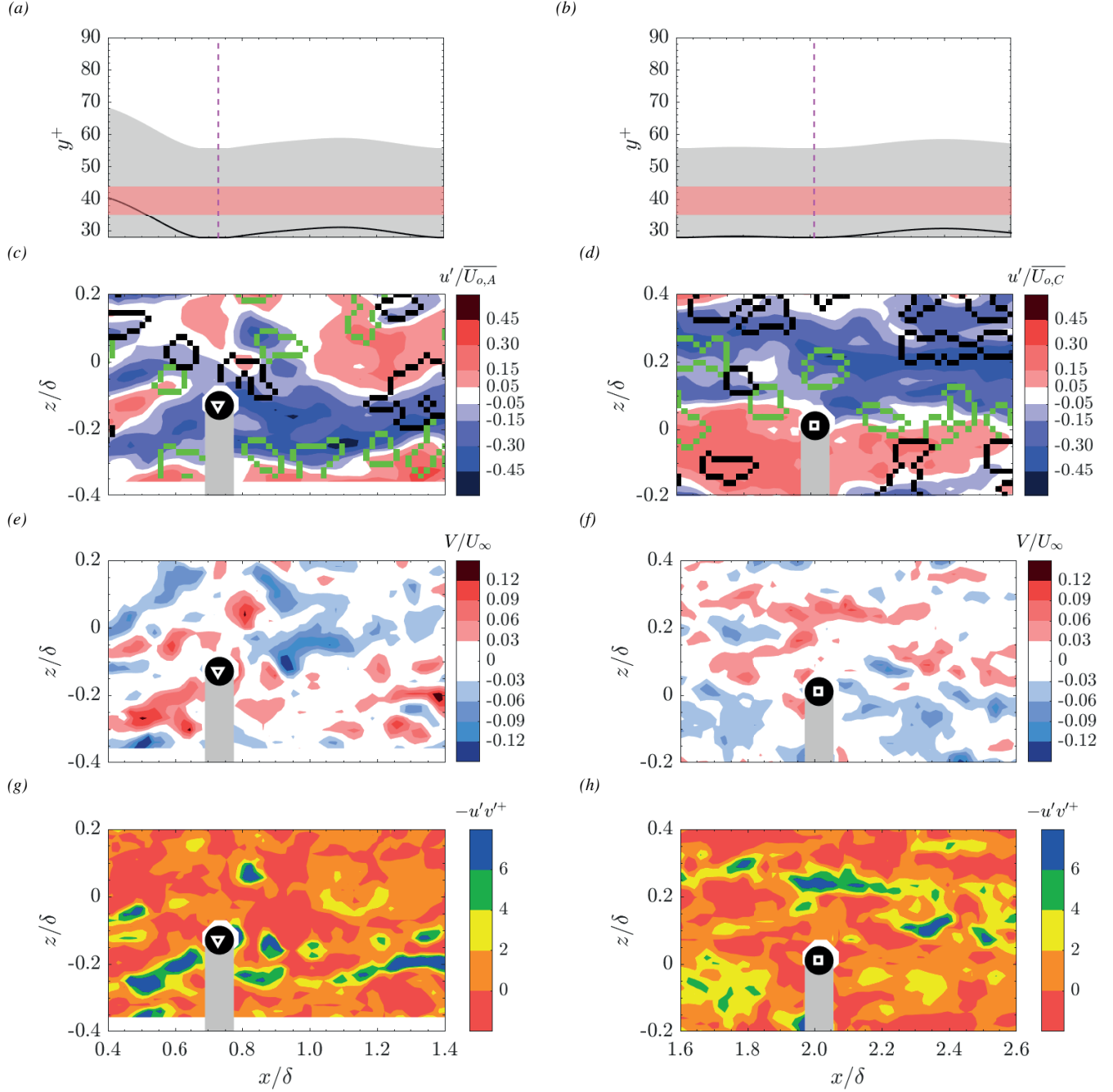
**Figure 4.** P1 at $Re_\tau = 670$ prior to lift-offs. Left $(a,c,e,g)$ and right $(b, d, f, h)$ columns represent two different runs. $(a, b)$ Black solid lines: sphere wall-normal trajectories. Red regions: laser sheet centered at $y/d = 0.7d$ or $y^+ = 40$. Grey regions: sphere. Magenta dotted lines: time instances of the contour plots below. $(c, d)$ Streamwise fluid fluctuating velocity, $(e, f)$ wall-normal fluid velocity, and $(g, h)$ negative Reynolds shear stresses contour plots, respectively. Black and green contours in $(c, d)$ represent the clockwise and counter-clockwise swirling structures.

that, although the mean shear lift decreases significantly after the sphere accelerates from rest, it still remains important. For reference, the value of $Re_{(p,f)}$ in Figure 4$a$ prior to its lift-off at $x/\delta \sim 0.7$ is smaller, around 130. Among all lifting events, however, no obvious $Re_{(p,f)}$ threshold value could be associated with the sphere lift-offs.

Based on all lift-off events across multiple runs, when $Re_\tau = 670$, more lift-offs were associated with surrounding Q2 events as in Figure 4$a$. By contrast, at the higher $Re_\tau$, more lift-off events were associated with a passing high momentum zone. To further validate our observations on the importance of large-scale coherent structures to sphere lift off, we computed two-point spatial correlation coefficients between sphere wall-normal velocity ($V_p$) and streamwise fluid velocity ($U$) for sphere P1 at both $Re_\tau$ across all runs using the following equation:

$$R_{V_p,U}(x, z) = \frac{1}{J-1} \sum_{j=1}^{J} \left( \frac{V_p(x_i,z_i)-\overline{V_p}}{\sigma_{V_p}} \right) \left( \frac{U(x_i\pm\Delta x,z_i\pm\Delta z)-\overline{U_o(y/d=0.7)}}{\sigma_U} \right) \tag{1}$$

The over-line represents the average quantity within the field of view across all runs; subscript 'i' represents the origin for spatial correlation which is the sphere centroid location; $\sigma$ represents the standard deviation; $\Delta$ represents the spatial displacement. To help reduce noise, the correlations were improved using a symmetry in $z$ such that the data at $z_i - \Delta z_a$ is reflected about $z_i$ to add to the correlation at $z_i + \Delta z_a$, for example. Even though sphere P1 moved in the $y-$direction, they did not rise completely above the laser sheet as shown in Figure 2. In the correlations, we therefore only consider results where the sphere intersects the laser sheet positioned at $y = 0.7d$ ($y^+ = 40$ and 80 for $Re_\tau = 670$ and 1300, respectively) throughout more than 90% of the SPIV field of view. The results are plotted in Figure 5$a$ and $b$ in the form of contour plots, with the origin ($x_i, z_i$) centered at the sphere centroid location. Here, $\delta x/\delta < 0$ and $\delta x/\delta > 0$ represent upstream and downstream of the sphere respectively. Due to the mirrored sphere shadow, the results above the black hemisphere are removed and plotted in grey. Note that even though the number of runs is insufficient to achieve smooth statistical convergence over the entire domain shown, the results are nevertheless useful in highlighting the predominant trends for large-scale particle-turbulence interaction.

Similar to the correlation between sphere and fluid streamwise velocities reported previously in Tee & Longmire (2021), $V_p$ is positively correlated to the streamwise fluid velocity over a long narrow streamwise region indicative of the long coherent fast and slow moving regions in the flow. The positive correlation is especially clear at $Re_\tau = 1300$. By separating the positive and negative sphere wall-normal velocity components (not shown here), we notice that these positive correlations derive mainly from the lift-off events or $V_p > 0$ when $u' > 0$. This discussion will be revisited later when we discuss the descending sphere. The stronger positive correlation observed at $Re_\tau = 1300$ is likely due to the greater effectiveness of relatively larger local shear leading to particle lift off. The weaker positive correlation observed at $Re_\tau = 700$ may also imply that, even though the instantaneous shear is important, lift-offs due to Q2 events ($V_p > 0$ when $u' < 0$), which would reduce the overall correlation value, are non-negligible. Nevertheless, the results suggest that large-scale coherent structures in the logarithmic region can strongly influence the wall-normal motion of the larger finite-size particles considered herein.
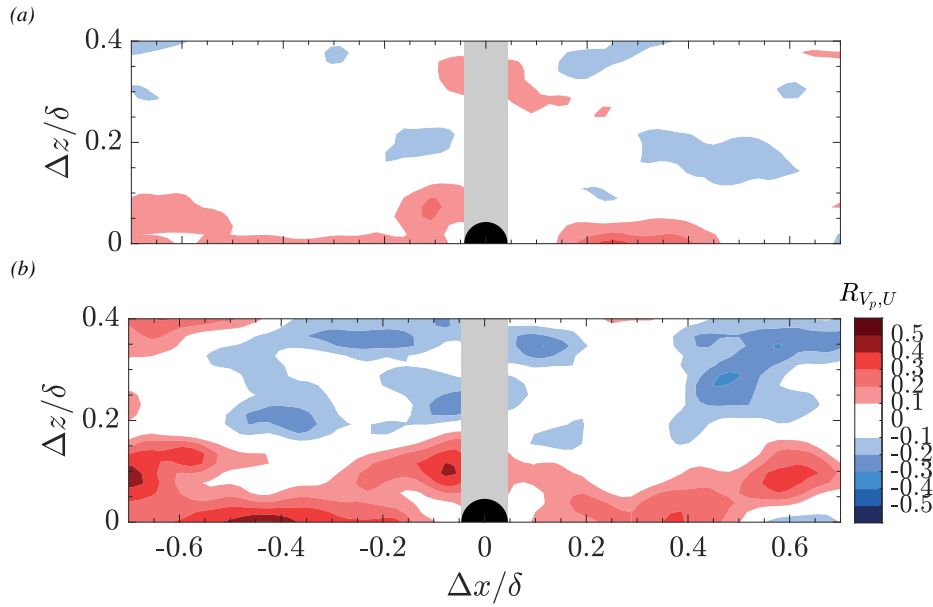
**Figure 5.** Two-point spatial correlation coefficients between the sphere wall-normal ($V_p$) and fluid streamwise velocities ($U$) for (*a*) P1 at $Re_\tau = 670$ and (*b*) P1 at $Re_\tau = 1300$.

As mentioned above, among all the lifting events observed within the tracked field of view of up to $\sim 5\delta$ (see Figure 2), the spheres always reached a short-lived peak in height within the logarithmic region followed by a descent. Since sphere P3 lifted only through Magnus effects and for very short times, the lifting and descent behavior appeared largely decoupled from coherent flow structures. Therefore, the following discussion will be limited to sphere P1 concerning the effect of turbulent fluid structures on sphere descents. Figure 6*a* and *b* show two examples of sphere P1 at $Re_\tau = 670$ after the upward sphere wall-normal velocity begins to decrease. In the first example on the left, prior to descending, the sphere is travelling within a long, slow moving zone (Figure 6*c*). The corresponding wall-normal fluid velocity field in Figure 6*e* suggests that the sphere is surrounded by small regions of downward and upward moving fluid at upstream and downstream locations respectively. A close look at the Reynolds stress plot in Figure 6*g* indicates the presence of a Q2 event immediately downstream of the sphere (where $u' < 0$ in Figure 6*c*) and $v' > 0$ in Figure 6*e*). This event, associated with the wake, persisted over the range $x/\delta \sim 1.4$ to $x/\delta \sim 1.8$. It is also notable from the time sequence of plots that the sphere is surrounded by upwash during much of its descent, and again during the subsequent ascent near the end of the field of view.

In the second example on the right, the sphere is also found in a slow moving zone (Figure 6*d*). Here, however, the sphere is surrounded by a larger region of upward moving fluid (see Figure 6*f*) than in the previous example. While there is no doubt that an impulse from downward moving fluid would aid a sphere's descent, the observed upwash suggests that even the upward moving fluid is insufficient to overcome the net downward force. Considering all of the descents observed in the current study, the sphere could be surrounded by either upward or downward moving fluid, implying that although a Q4 event or a downward moving fluid might be important, it is likely not the main contributor in causing the sphere to descend. More specifically, the overall impulse
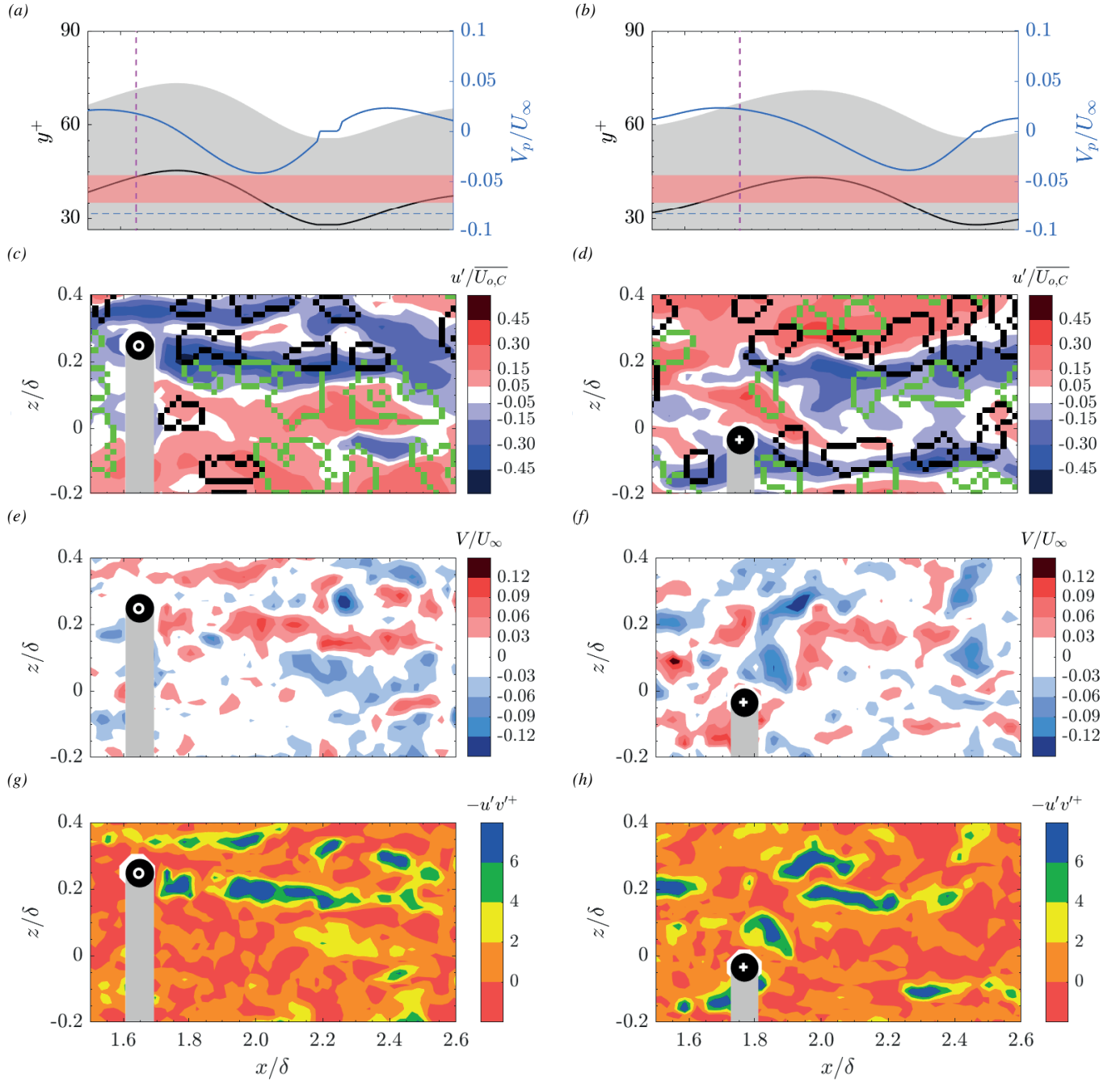
**Figure 6.** P1 at $Re_\tau = 670$ prior to descent. Left (*a,c,e,g*) and right (*b, d, f, h*) columns represent two different runs. (*a, b*) Black solid lines (left axis): sphere wall-normal trajectories. Blue solid and dashed lines (right axis): sphere wall-normal velocity and settling velocity respectively. Red regions: laser sheet centered at $y/d = 0.7d$ or $y^+ = 40$. Grey regions: sphere. Magenta dotted lines: time instances of the contour plots below. (*c, d*) Streamwise fluid fluctuating velocity, (*e, f*) wall-normal fluid velocity, and (*g, h*) negative Reynolds shear stresses contour plots, respectively. Black and green contours in (*c, d*) represent the clockwise and counter-clockwise swirling structures.

contributed by such events is relatively small compared to the steady impulse of gravity.

In a study on smaller spheres, Baker & Coletti (2021) reported that particle descents were prompted by both gravity and negative shear, and were not correlated with sweep events. In our study, the effects of negative shear lift on descents of larger spheres with higher Stokes numbers could not be quantified. However, among many runs investigated, we did not observe any obvious trends in the fluid structures associated with sphere descents. Our correlation analysis on $V_p$ and $U$ based on Equation 1, focusing only on descending particles, also did not show significant correlations with negative $u'$ which might be associated with a temporary decrease in shearing. Thus, variations in shear due to passing coherent structures are likely less significant in initiating or driving sphere descents. As the sphere moves upward away from the wall, it is also accelerating in the streamwise direction due to the additional momentum from the streamwise fluid above the wall (see Tee et al., 2020). This causes the sphere relative velocity to decrease in general. At the same time, it is also moving away from the region of strongest mean shear. As discussed in Tee et al. (2020), the sphere never rises above the logarithmic region. Hence, without additional upward momentum from the flow structures, an ascending sphere that loses its upward force (and impulse) after ascending will always descend towards the wall likely due to a decrease in positive wall-normal shear lift. Therefore, it appears to us that the dominant factor in driving the sphere back towards the wall is the downward gravity.

In Tee et al. (2020), we reported that in some runs, sphere P1, especially at $Re_\tau = 1300$, occasionally descended with wall-normal velocity stronger than its settling velocity which must be prompted by the fluid structures. Such behavior is observed in roughly 6 out of 30 descents of sphere P1 at $Re_\tau = 1300$ and none at the lower $Re_\tau$ case in current study. In these examples, the sphere typically lifted off to heights significantly above that of the laser sheet, and therefore, we do not have fluid data surrounding the sphere near the start of its descent. Nevertheless, the occasional higher downward velocities suggest that smaller-scale turbulent fluctuations and shear effects due to larger structures can be important at $Re_\tau = 1300$. At this higher flow Reynolds number, the local turbulence intensity and shearing can be higher than at $Re_\tau = 670$.

## 4. Conclusions

Individual spheres with diameters of 56 and 116 viscous units and specific gravities of 1.006 (P1) and 1.152 (P3) were released from rest at both $Re_\tau = 670$ and 1300 and tracked over a streamwise distance up to $x \approx 5\delta$ using a 3D particle tracking technique. Stereoscopic particle image velocimetry experiments were conducted simultaneously in streamwise-spanwise planes at various streamwise and wall-normal positions to quantify the fluid motion surrounding the moving sphere. In this paper, the fluid motions surrounding ascending and descending spheres were discussed.

Upon release, when the mean shear lift force is larger than the net buoyancy force, the less dense sphere P1 lifted off from the wall in almost all runs. This sphere underwent multiple lift-off events,

including saltation and resuspension, with stronger lift-off magnitudes observed at higher $Re_\tau$. Throughout its trajectory, the lifting sphere translated with very weak or minimal rotation about any axis. By correlating the sphere wall-normal velocity and the fluid streamwise velocity, the results also suggest that the high and low momentum regions in the logarithmic layer have important effects on sphere lift-offs. Most importantly, the presence of a high momentum region increases the local shear and provides the sphere with sufficient lift force to move away from the wall. Moreover, in agreement with the studies by van Hout (2013) and Baker & Coletti (2021) for example, our results also show that upwash or ejection events can be important to the lift-off of this sphere in some cases. This sphere never lifted above the logarithmic layer and always descended towards the wall after reaching a peak height. Our analysis suggests that these descents are not prompted by sweep events or local variations in fluid shear due to passing low or high momentum regions. Instead, the descents are likely caused by the gravitational force which becomes increasingly important as the spheres lose their positive upward force after ascending above the wall.

On the other hand, the denser wall-interacting sphere P3 did not lift off upon release but first slid along the wall with minimal rotation. After propagating downstream by about $1.5\delta$, this sphere began to roll forward (while partially slipping) and accelerated again. The rolling motion induced significant Magnus lift causing the sphere to lift off of the wall repeatedly. Since this sphere was significantly denser than sphere P1, its lift-off heights were always small, less than $0.2d$, and it descended towards the wall almost immediately due to gravity. Thus, its wall-normal motions were largely decoupled from the turbulent motions.

## Acknowledgements

## References

Ahmadi, F., Ebrahimian, M., Sanders, R. S., & Ghaemi, S. (2019). Particle image and tracking velocimetry of solid-liquid turbulence in a horizontal channel flow. *International Journal of Multiphase Flow*, *112*, 83–99.

Baker, L. J., & Coletti, F. (2021). Particle–fluid–wall interaction of inertial spherical particles in a turbulent boundary layer. *Journal of Fluid Mechanics*, *908*.

Barros, D., Hiltbrand, B., & Longmire, E. K. (2018). Measurement of the translation and rotation of a sphere in fluid flow. *Experiments in Fluids*, *59*(6), 104.

Bellani, G., Byron, M. L., Collignon, A. G., Meyer, C. R., & Variano, E. A. (2012). Shape effects on turbulent modulation by large nearly neutrally buoyant particles. *Journal of Fluid Mechanics*, *712*, 41–60.

Brandt, L., & Coletti, F. (2021). Particle-laden turbulence: Progress and perspectives. *Annual Review of Fluid Mechanics*, *54*.

Costa, P., Brandt, L., & Picano, F. (2020). Interface-resolved simulations of small inertial particles in turbulent channel flow. *Journal of Fluid Mechanics*, *883*.

Crowe, C. T. (2005). *Multiphase flow handbook*. CRC press.

Francis, J. R. D. (1973). Experiments on the motion of solitary grains along the bed of a water-stream. In *Proceedings of the royal society of london. series a, mathematical and physical sciences* (Vol. 332, p. 443-471). The Royal Society London.

Ganapathisubramani, B., Longmire, E. K., & Marusic, I. (2003). Characteristics of vortex packets in turbulent boundary layers. *Journal of Fluid Mechanics*, *478*, 35.

Hall, D. (1988). Measurements of the mean force on a particle near a boundary in turbulent flow. *Journal of Fluid Mechanics*, *187*, 451-466.

Kabsch, W. (1976). A solution for the best rotation to relate two sets of vectors. *Acta Crystallographica Section A: Crystal Physics, Diffraction, Theoretical and General Crystallography*, *32*(5), 922–923.

Klein, S., Gibert, M., Bérut, A., & Bodenschatz, E. (2013). Simultaneous 3D measurement of the translation and rotation of finite-size particles and the flow field in a fully developed turbulent water flow. *Measurement Science and Technology*, *24*(2), 024006.

Mathai, V., Neut, M. W., van der Poel, E. P., & Sun, C. (2016). Translational and rotational dynamics of a large buoyant sphere in turbulence. *Experiments in Fluids*, *57*(4), 51.

Sciacchitano, A., Scarano, F., & Wieneke, B. (2012). Multi-frame pyramid correlation for time-resolved PIV. *Experiments in Fluids*, *53*(4), 1087–1105.

Soldati, A., & Marchioli, C. (2009). Physics and modelling of turbulent particle deposition and entrainment: Review of a systematic study. *International Journal of Multiphase Flow*, *35*(9), 827-839.

Sumer, B. M., & Oğuz, B. (1978). Particle motions near the bottom in turbulent flow in an open channel. *Journal of Fluid Mechanics*, *86*(1), 109-127.

Sutherland, A. J. (1967). Proposed mechanism for sediment entrainment by turbulent flows. *Journal of Geophysical Research*, *72*(24), 6183-6194.

Tan, Y. M., & Longmire, E. K. (2017). Recovery of vortex packet organization in perturbed turbulent boundary layers. *Physical Review Fluids*, *2*(10), 104602.

Tee, Y. H. (2021). *Resolving particle dynamics in turbulent wall-bounded flow* (Unpublished doctoral dissertation). University of Minnesota.

Tee, Y. H., Barros, D. C., & Longmire, E. K. (2020). Motion of finite-size spheres released in a turbulent boundary layer. *International Journal of Multiphase Flow*, *133*, 103462.

Tee, Y. H., & Longmire, E. K. (2021). Time-resolved sphere and fluid motions in turbulent boundary layers. In *14th international symposium on particle image velocimetry* (Vol. 1).

van Hout, R. (2013). Spatially and temporally resolved measurements of bead resuspension and saltation in a turbulent water channel flow. *Journal of Fluid Mechanics*, *715*, 389-423.

van Hout, R., Eisma, J., Elsinga, G. E., & Westerweel, J. (2018). Experimental study of the flow in the wake of a stationary sphere immersed in a turbulent boundary layer. *Physical Review Fluids*, *3*(2), 024601.

Zeng, L., Balachandar, S., Fischer, P., & Najjar, F. (2008). Interactions of a stationary finite-sized particle with wall turbulence. *Journal of Fluid Mechanics*, *594*, 271–305.

Zimmermann, R., Gasteuil, Y., Bourgoin, M., Volk, R., Pumir, A., & Pinton, J.-F. (2011). Tracking the dynamics of translation and absolute orientation of a sphere in a turbulent flow. *Review of Scientific Instruments*, *82*(3), 033906.